

Elastic impedance inversion of multichannel seismic data from unconsolidated sediments containing gas hydrate and free gas

Shaoming Lu* and George A. McMechan*

ABSTRACT

The elastic properties of hydrated sediments are not well-known, which leads to inaccuracy in the evaluation of the amount of gas hydrate worldwide. Elastic impedance inversion is useful in estimating the elastic properties of sediments containing gas hydrate, or free gas trapped beneath the gas hydrate, from angle-dependent P-wave reflections.

We reprocess the multichannel U.S. Geological Survey seismic line BT-1 from the Blake Ridge off the east coast of North America to obtain migrated common-angle aperture data sets, which are then inverted for elastic impedance. Two new algorithms to estimate P-impedance and S-impedance from the elastic impedance are developed and evaluated using well-log data from Ocean Drilling Program (ODP) Leg 164; these new algorithms are stable, even in the presence of modest noise in the data.

The V_s/V_p ratio, Poisson's ratio, and Lamé parameter terms $\lambda\rho$ and λ/μ are estimated from the P-impedance and S-impedance. The hydrated sediments have high elastic impedance, high P-impedance, high S-impedance, high $\lambda\rho$, slightly higher V_s/V_p ratio, slightly lower Poisson's ratio, and slightly lower λ/μ values com-

pared to those of the surrounding unhydrated sediments. The sediments containing free gas have low elastic impedance, low P-impedance, nonanomalous background S-impedance, high V_s/V_p ratio, low Poisson's ratio, low $\lambda\rho$, and low λ/μ values. We conclude that some parameters such as V_s/V_p ratio, Poisson's ratio, and λ/μ , although they help identify the free-gas charged layers, cannot differentiate between the hydrated sediments and nonhydrated sediments when gas hydrate concentration is low, and cannot differentiate between the hydrated sediments and free-gas charged sediments when the gas hydrate concentration is high.

Three distinct layers of gas hydrate are interpreted as being caused by gas hydrates with gas of different molecular weights, with correspondingly different stability zones in depth. Free gas appears to be present below the two deeper gas-hydrate layers, but not below the shallowest one because the lack of a trapping structure. The gas hydrate has an average concentration of ~3–5.5% by volume, and is highest (9%) at the base of the lower gas hydrate stability zone. The free-gas concentration ranges from 1 to 8% by volume, and is most developed beneath the local topographic high of the ocean bottom.

INTRODUCTION

Large amounts of natural gas hydrate can form and remain stable under appropriate conditions of high pressure, low temperature, and high gas concentration in oceanic sediments (Sloan, 1998a). Gas hydrates may represent a huge untapped source of energy, but this is uncertain in view of recent results on the distribution of gas hydrates in sediments (Laherrère, 2000). In any case, no economic gas production from gas hydrate is expected within 10 to 30 years (Grauls, 2001). The amount of methane trapped beneath the gas-hydrate stability zone (GHSZ) in the form of free gas is also potentially large

(Dickens et al., 1997), and is considered as a secondary objective that might be produced as early as 2005 (Grauls, 2001), but this is also speculative because of the difficulties in estimating resource potential (Laherrère, 2000). The uncertainties arise from the fact that little is known about the elastic properties of hydrated sediments, although the elastic properties of pure gas hydrate are well known (Sloan, 1998b). The motivations to obtain a better understanding of the seismic properties of gas hydrate (in addition to its economic potential) are its role in global climate change, as submarine geologic hazards, and as drilling hazards (Kvenvolden, 1998).

Manuscript received by the Editor May 13, 2002; revised manuscript received April 19, 2003.

*Center for Lithospheric Studies, University of Texas at Dallas, P.O. Box 830688, Richardson, Texas 75083-0688, E-mail: mcmec@utdallas.edu; shaom@utdallas.edu.

© 2004 Society of Exploration Geophysicists. All rights reserved.

Most oceanic natural gas hydrates are studied through their bottom-simulating reflectors (BSRs), which are seismic reflections that locally parallel the sea-floor reflection, and have reverse polarity compared to the sea-floor reflection. The BSR is believed to be caused by the impedance contrast associated with free gas beneath the base of the GHSZ and so marks the base of the GHSZ (Tinivella and Lodolo, 2000). A double BSR pattern was observed both in the Oregon continental margin [where it is interpreted as a temporary feature caused by changing sediment thickness caused by tectonic processes (Tréhu et al., 1999)] and in the Norwegian continental margin [where it is interpreted as a stable feature caused by different gas-hydrate compositions having different stability zones in depth (Andreassen et al., 2000)]. The latter model is consistent with the observations below.

In a previous paper (Lu and McMechan, 2002), a single-channel seismic line USGS95-1 and well-logs from Sites 994, 995, and 997 of Ocean Drilling Program (ODP) Leg 164 (Figure 1) are used to invert for acoustic impedance (AI), from which the distribution and concentration of gas hydrate and free gas at the Blake Ridge are estimated. Elastic as well as acoustic properties can be derived from multichannel seismic data by elastic impedance (EI) inversion. Thus, we are able to study the elastic properties of hydrated sediments and correlate these to an independently determined distribution and concentration of gas hydrate.

EI inversion has been very useful in estimating the elastic properties from angle-dependent P-wave reflections. EI inversion has advantages over traditional amplitude variation with offset (AVO) inversion when the wavelet varies with offset (Cambois, 2000). In this paper, we use the concept of EI (Connolly, 1999), and invert time-migrated common-angle aperture (CAA) data sets of multichannel seismic line BT-1 from the Blake Ridge (Figure 1) for EI. We use the well-log information from ODP Sites 995 and 997 because these are the closest wells that have shear logs. We then develop and evaluate algorithms to estimate P-impedance and S-impedance from EI. The algo-

rithms are tested with EI calculated from well-logs from Site 997, and are then applied to the seismic EI sections obtained by inversion of CAA seismic data from line BT-1. V_s/V_p ratio, Poisson's ratio, and Lamé parameter terms are estimated from the P- and S-impedance sections. Gas hydrate and free gas affect different attributes differently and so allow their identification. We use calibrations developed by Lu and McMechan (2002) to estimate the distribution and concentration of gas hydrates and free gas for the seismic line BT-1. Finally, a comprehensive interpretation of all the results is made.

GEOLOGIC SETTING

The Blake Ridge is a pronounced topographic sedimentary feature on the southeastern U.S. continental margin (Figure 1). It is a major Neogene and Quaternary sediment ridge that consists of hemipelagic silt-rich and clay-rich deposits (Wehner et al., 2000). The sediments are lithologically homogeneous, and were deposited by the southward flowing western boundary undercurrent that carries materials laterally along the continental margin (Paull and Matsumoto, 2000). A rough topographic depression, which is considered to be a collapse structure that appears to have been formed by gas hydrate-related processes, exists at the crest of the ridge (Dillon et al., 2001).

Well-developed BSRs in the crest of the ridge cover an area of about 26 000 km² (Matsumoto, 2000). The isopach of the interval from the sea floor to the base of GHSZ ranges in thickness from zero along the northwestern edge of the continental shelf to a maximum of 700 m along the eastern edge of the Blake Ridge (Collett and Ladd, 2000).

SEISMIC DATA REPROCESSING PROCEDURE AND RESULTS

Seismic line BT-1 was acquired for the U.S. Geological Survey by Geophysical Service Inc. (GSI) in 1974 using tuned air-gun array sources and 48 channel, nonlinear streamers

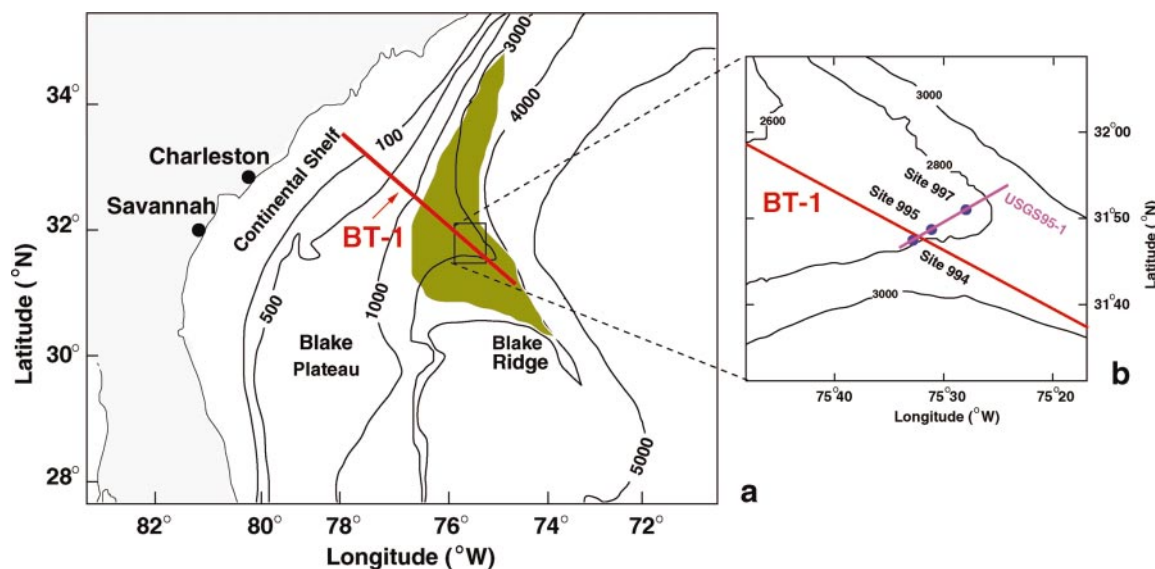


FIG. 1. Location of the Blake Ridge, the seismic line BT-1, and three drill sites (994, 995 and 997) of ODP Leg 164. In (a), the green area corresponds to the extent of the BSRs (after Paull et al., 1996); bathymetric contours are in meters. The heavy lines in (b) are the locations of seismic lines BT-1 (in red) and USGS95-1 (in magenta); the latter goes through ODP drill sites 994, 995 and 997 (the blue dots).

with a length of 3600 m. The line provides 36-fold coverage with 50-m common midpoint (CMP) intervals (Lee et al., 1993, 1994).

Reprocessing procedure

The goal of the reprocessing of line BT-1 is to maintain accurate amplitudes, so the processing flow is limited to as few steps as possible. Water column multiples are not a problem because they arrive at times later than those we are interested in. The amplitude compensation for the geometrical spreading uses rms velocity that is picked interactively in semblance windows during velocity analysis. The reflectors are fairly flat, so dip moveout makes little difference to the results and is not used. An 8-55-Hz Butterworth time-variant bandpass filter is applied after minimum phase Wiener-Levinson predictive deconvolution. A stacked section is produced for each CAA data set after normal moveout correction; the stacked amplitude at each time sample is divided by the number of the stack fold at that time sample to compensate for the differing number of traces present after muting of the normal moveout stretch. Finally, Kirchhoff time migration is applied to each CAA stacked section. The migrated CAA sections are input to EI inversion.

Reprocessing results

The outputs of the reprocessing are time-migrated CAA data sets (Figure 2). The incident angles range from 0° to 32° . Laterally, the BSR has the highest amplitude in the middle of the

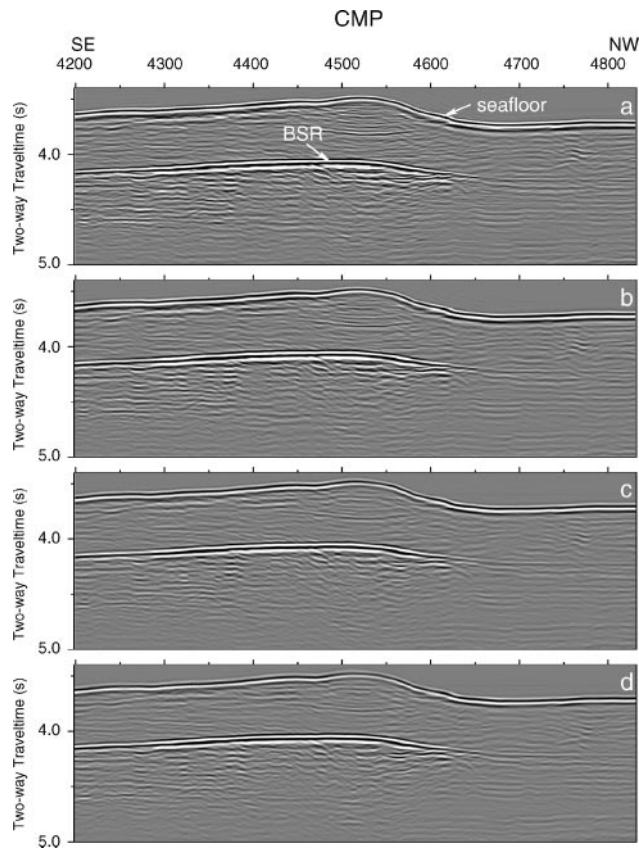


FIG. 2. Time-migrated CAA data sets of Line BT-1. The common angle apertures are (a) 0° – 8° , (b) 8° – 16° , (c) 16° – 24° , and (d) 24° – 32° . The horizontal scale is 5 km/100 CMPs.

section, which is beneath a local high in the sea-floor topography (Figure 2). The amplitude of the BSR decreases away from the middle of the section, and almost disappears at the right side of the section. No obvious amplitude blanking above the BSR can be observed in Figure 2, although blanking has been interpreted in other lines in this area (Lee et al., 1993, 1994). The BSR has high amplitude in all CAA data sets, and shows significant variations with offset (Figure 3). It is these variations that make the next step, EI inversion, feasible.

ELASTIC IMPEDANCE AND INVERSION

Elastic impedance

The concept of EI has been very useful in rock-property analysis and interpretation (Savic et al., 2000; Mallick, 2001). Connolly (1999) defined EI as an angle-dependent weighted product of P-velocity (V_p), S-velocity (V_s), and density (ρ):

$$EI(\theta) = V_p^{(1+\tan^2\theta)} V_s^{(-8K\sin^2\theta)} \rho^{(1-4K\sin^2\theta)}, \quad (1)$$

where K is the average V_s^2/V_p^2 value over the two layers above and below the interface, and θ is the incident angle. By equation (1), the units of EI change with the incident angle; Whitcombe (2002) shows that EI can be normalized to give the same units (i.e., ρV) as AI. The definition (1) is derived as a second-order linearization of the Zoeppritz equation for the P-to-P reflection coefficient equation (Connolly, 1999). With this definition, EI is a generalization of AI [i.e., $AI = EI(0^\circ)$]; the reflection coefficient $R(\theta)$ can be expressed in the same form as the normal incidence AI reflection coefficient:

$$R(\theta) = \frac{EI_2 - EI_1}{EI_2 + EI_1}. \quad (2)$$

Thus, the Constrained Sparse Spike Inversion (CSSI) developed for AI inversion (e.g., Helgesen et al., 2000) that was used by Lu and McMechan (2002) can also be used for EI inversion.

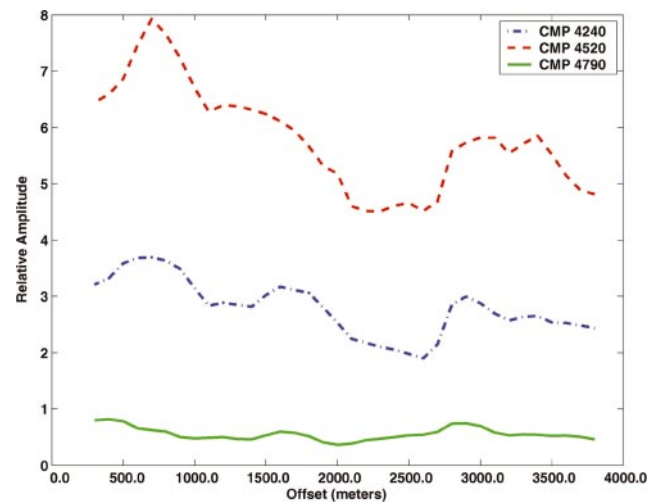


FIG. 3. Lightly smoothed amplitude variation with offsets curves of CMP gathers 4240, 4520, and 4790. These curves are obtained by picking the maximum values of the absolute amplitude in a small time window that includes the BSR (Figure 2). The local amplitude variations may be caused by interference between the BSR reflections and those from the underlying stratigraphy.

Elastic impedance inversion

CSSI finds EI values within prescribed constraints by minimizing the objective function

$$F = \sum_i |r_i|^p + \lambda^q \sum (d_i - s_i)^q \quad (3)$$

over all times i , where r_i is the reflection coefficient (which is a function of EI), λ is the data mismatch weighting factor, d_i is one of the traces of the migrated CAA data set, and s_i is the corresponding synthetic trace. Setting $p \approx 1$ (the L_1 norm) enhances stability where there may be outliers in the data (Claerbout and Muir, 1973; Menke, 1984, 190–194), such as in a spike reflection coefficient series. Setting $q = 2$ (the L_2 norm) is appropriate for fitting smooth data with nearly Gaussian statistics (Menke, 1984, 36–39), such as seismic traces with modest noise. In most cases, the default values for $p (= 0.9)$ and $q (= 2)$ are near optimal to invert most seismic data (Jason Geosystems, 1999). The data mismatch weighting function λ is used to balance the contribution of the two terms in equation (3), as they can not both be minimized simultaneously. If λ is too small, the inverted results do not explain the data, and the data mismatch will be large; if λ is too large, noise as well as the data are fitted, and the signal-to-noise ratio will be low. Quality control panels are used to determine the optimum value for λ ; we use λ values between 13 and 18, which are different for each CAA data set.

ESTIMATION OF P-IMPEDANCE AND S-IMPEDANCE FROM ELASTIC IMPEDANCE

The concept of EI will be more useful if we can estimate the P- and S-impedances (ρV_p and ρV_s) from EI. Several algorithms can be used.

Three algorithms for estimating P-impedance and S-impedance

Algorithm 1 is directly from the definition of EI. We take the natural log of both sides of equation (1), and get

$$\ln(EI) = (1 + \tan^2 \theta) \ln(V_p) + (-8K \sin^2 \theta) \ln(V_s) + (1 - 4K \sin^2 \theta) \ln(\rho). \quad (4)$$

This algorithm requires at least three independent angle data sets to estimate the three unknowns V_p , V_s , and ρ . Mallick et al. (2000) showed with synthetic data that algorithm 1 can recover V_p , V_s , and ρ accurately when there is no noise in the EI. In the presence of only 2% random noise in the EI, algorithm 1 could not recover the original velocity and density model, but still could estimate ρV_p and ρV_s , because the impedance is preserved in the solution even though V_p , V_s , and ρ individually are not.

Using the small angle approximation $\tan^2 \theta \approx \sin^2 \theta$, and the empirical relation (Appendix A)

$$4K \sin^2 \theta \ln(\rho) \approx \sin^2 \theta \ln(\rho) - 6K(0.25 - K) \left(\frac{1}{aK} - \frac{K}{b} \right) \sin^2 \theta, \quad (5)$$

algorithm 1 becomes algorithm 2, which is

$$\ln(EI) \approx \ln(\rho V_p)(1 + \sin^2 \theta) - 8K \ln(\rho V_s) \sin^2 \theta - 6K(0.25 - K) \left(\frac{1}{aK} - \frac{K}{b} \right) \sin^2 \theta. \quad (6)$$

Here, coefficients $a = 8.0$ and $b = 0.5$ for K less than 0.25, and $a = 3.0$ and $b = 3.0$ for K larger than 0.25. Equation (5) is a reasonable approximation [for example, the average absolute percent error between EIs of $\theta = 30^\circ$ from equations (6) and (1) is 1.47%, using the V_p log, the V_s log, and the ρ log from Site 997 (see Lu and McMechan, 2002)] for all K values between 0.0 and 0.8. Algorithm 2 requires at least two independent angle data sets to estimate ρV_p and ρV_s .

If we know the ρV_p profile from elsewhere (for example, from acoustic impedance inversion for $\theta \approx 0^\circ$, or from well logs), we have algorithm 3, which is

$$\ln(\rho V_s) \approx \frac{\ln(\rho V_p)(1 + \sin^2 \theta) - \ln(EI)}{8K \sin^2 \theta} - \frac{3}{4}(0.25 - K) \left(\frac{1}{aK} - \frac{K}{b} \right). \quad (7)$$

Only one finite-angle data set ($\theta \neq 0^\circ$) is required to estimate ρV_s with algorithm 3.

Well-log data synthetic results

To evaluate the three algorithms in equations (4), (6), and (7), we generate synthetic EI data using equation (1) for several incidence angles from the V_p log, the V_s log, and the ρ log from Site 997. We then invert for ρV_p and ρV_s from EI by using these three algorithms. As the well logs inherently contain the low-frequency background trends, the trends do not have to be separately estimated and inserted into the well-log EI data (for these tests only). When we use the exact EI calculated from the well-log data (no noise), algorithm 1 [equation (4)] can fully recover ρV_p and ρV_s (not shown), as Mallick et al. (2000) did. If we add 7% random noise to the calculated EI and invert for ρV_p and ρV_s , the inverted ρV_s is unstable and contains unreasonable values (Figures 4c and 4d). The recovery of ρV_p (Figure 4a) is very good, especially after smoothing to reduce the effect of the noise (Figure 4b); smoothing cannot overcome the errors in the inverted ρV_s (Figure 4d).

Better results may be obtained by using constraints during inversion (which is a common practice), but our purpose here is to compare the different algorithms, so no constraints were used. Figures 4c and 4d show that algorithm 1 is very sensitive to noise in the inversion of ρV_s ; Mallick (2001) has a similar conclusion. Thus, we will not use this algorithm to estimate ρV_p and ρV_s from EI sections.

Algorithm 2 [equation (6)] does a much better job than algorithm 1 in the inversion of ρV_s when noise is present (Figure 5c); this is clearer after smoothing (Figure 5d). Algorithm 2 gives a similar inverted ρV_p profile to that from algorithm 1 (compare Figures 5a and 5b with Figures 4a and 4b).

Algorithm 3 [equation (7)] assumes that ρV_p is already known, and solves only for ρV_s . First, we again add noise into EI, and use the exact ρV_p calculated from the well logs. The inverted ρV_s is much better than that of algorithm 2, both before (Figure 6a) and after (Figure 6b) smoothing. Smoothing

improves the estimation of ρV_s . Next, we add 7% noise to both EI and to the known ρV_p . The inverted ρV_s (Figures 7a and 7b) is still better than that of algorithm 2 (Figures 5c and 5d). If in Figure 7b, 5% rather than 7% noise is added, δ drops from 0.110 to 0.084 $10^6 \text{kg/m}^2/\text{s}$, and the δ between these two best-fit solutions is 0.034 $10^6 \text{kg/m}^2/\text{s}$. Thus, the solution itself is relatively

stable as noise changes, but the uncertainty in the solution increases as noise increases.

BT-1 DATA RESULTS

Before EI inversion of the BT-1 seismic data, we compute EI logs [according to equation (1)] for those angles that are

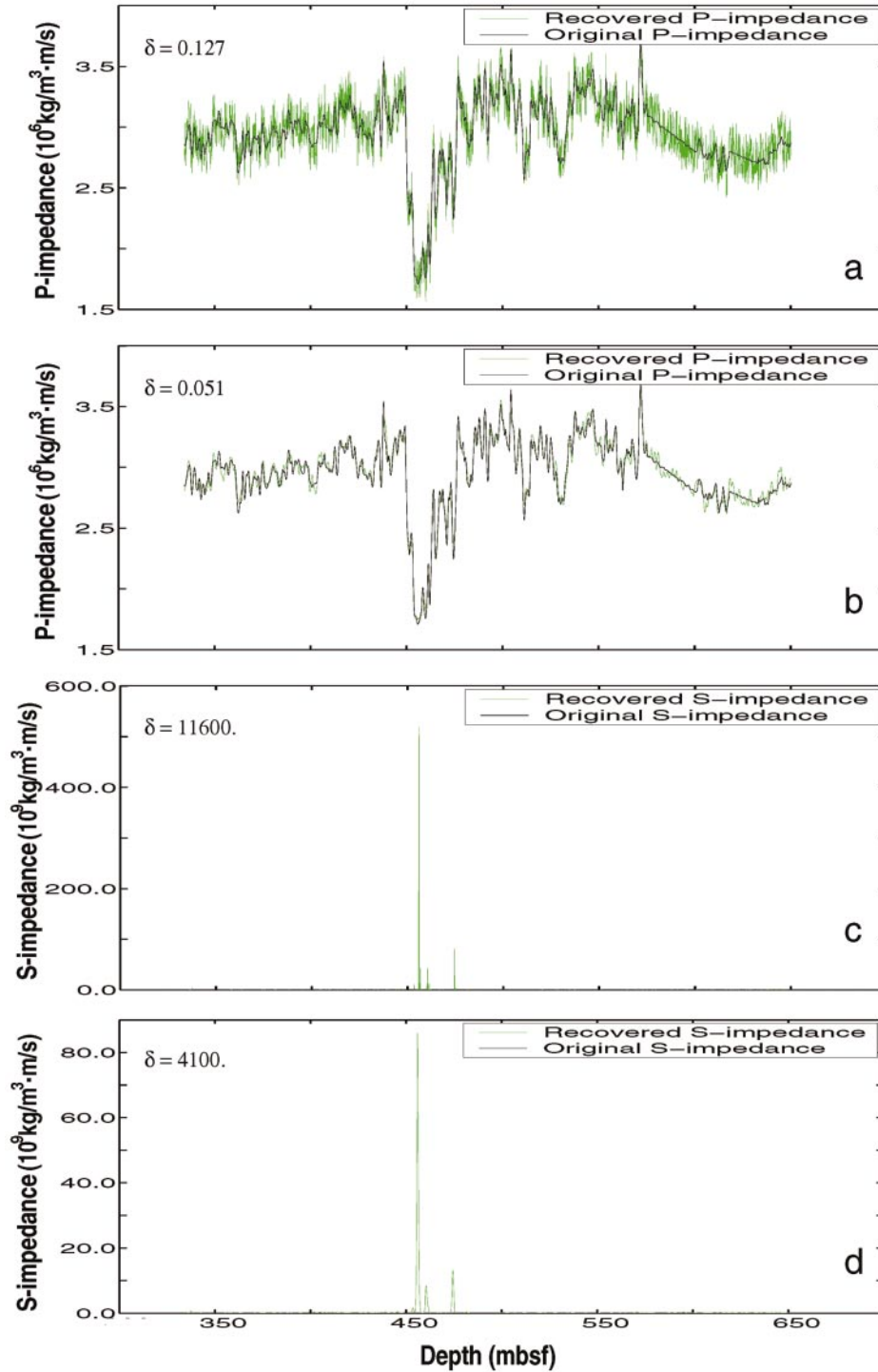


FIG. 4. Parameters ρV_p and ρV_s inverted from EI with 7% random noise using algorithm 1: (a) is the inverted ρV_p before smoothing, (b) is the inverted ρV_p after smoothing, (c) is the inverted ρV_s before smoothing, and (d) is the inverted ρV_s after smoothing. The input EI was constructed from the well logs of Site 997. A 21-point triangular smoothing was used, δ is the standard deviation.

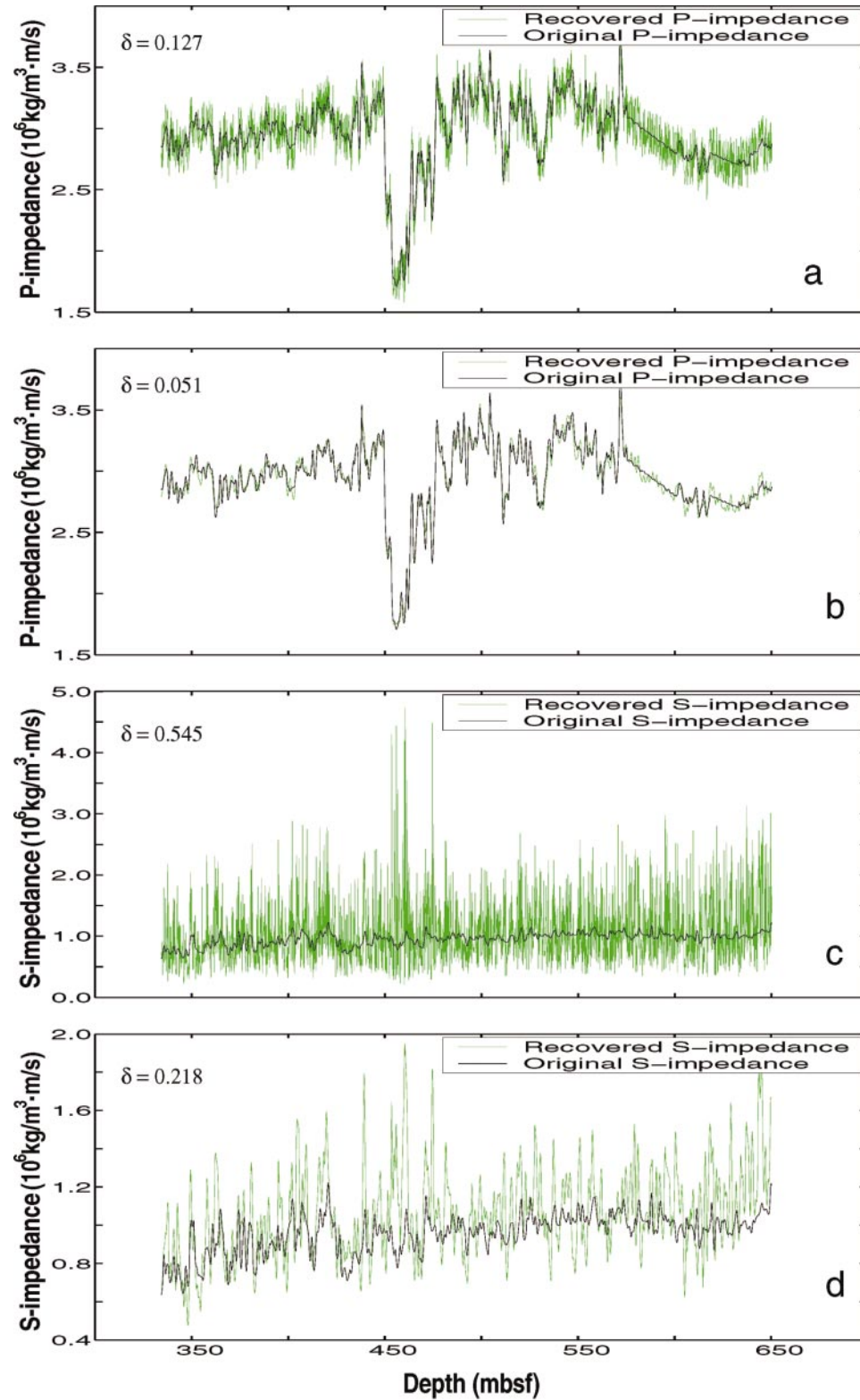


FIG. 5. Parameters ρV_p and ρV_s inverted from EI with 7% random noise using algorithm 2 [equation (6)]: (a) is the inverted ρV_p before smoothing, (b) is the inverted ρV_p after smoothing, (c) is the inverted ρV_s before smoothing, and (d) is the inverted ρV_s after smoothing. The input EI was constructed from the well logs of Site 997. A 21-point triangular smoothing was used; δ is the standard deviation.

present in the migrated CAA sections by using corrected V_p , V_s , and ρ logs from Sites 995 and 997. (Site 994 does not have a V_s log and so is not used in the inversion). The computed EI logs are used for two purposes: wavelet estimation, and obtaining the low-frequency EI model. Since the wavelet varies with offset, a wavelet for each migrated CAA data set is estimated using the computed EI log for the corresponding incidence angle. The wavelets estimated therefore closely match the amplitude, frequency, and phase of their respective CAA data sets. Also, since the outputs of the CSSI are band-limited EI sections, the low-frequency component that is missing in the band-limited EI sections has to be estimated and inserted.

A low-frequency EI model cannot be obtained directly by smoothing and interpolating the synthetic EI logs from Sites 995 and 997, as these are ~ 3 and ~ 10 km, respectively, off line BT-1. However, the relations between the low-frequency V_p , V_s , and ρ at Sites 995 and 997 are expected to be very similar along line BT-1 as the geologic environment varies slowly; in any case, these well logs are the only available constraints for V_s and ρ . Thus, we use a combination of the 2D V_p model from the seismic velocity analysis (weighted 70%) and the average of the smoothed (0–1 Hz) V_p profiles from the two wells (weighted 30%) for the low-frequency V_p model. Then, the low-frequency 2D V_s and ρ models are obtained from the average low-frequency V_p - V_s and V_p - ρ relations from the logs.

Elastic impedance

Figure 8 shows the four EI sections obtained from the EI inversion of the four CAA data sets in Figure 2. Prominent

features in all the EI sections are two pairs of high-over-low impedance layers, labeled H1, L1, H2, and L2 in Figure 8a. The two pairs are unexpected, and are interpreted below in terms of alternating gas-hydrate and free-gas layers.

EI changes with incidence angle are most visible in L1 and H2; as the incidence angle increases, the magnitude of the EI values in L1 becomes smaller, and those in H2 become larger. These changes in the EI AVO are quantified below as the result of changing hydrocarbon concentration.

ρV_p and ρV_s

Testing with well-log data in the foregoing section shows that algorithms 2 and 3 can recover ρV_p and ρV_s fairly well, even when noise is present. Therefore, we now apply these two algorithms to the BT-1 seismic data. This time, we use constraints developed with the ρV_s logs of Sites 995 and 997 for the inversion of ρV_s . No constraints are needed for the inversion of ρV_p , since it is relatively insensitive to noise. Figure 9 shows the ρV_p and ρV_s sections inverted from the EI sections (Figure 8) using algorithm 2. The ρV_p projected from Site 994 is overlain with the inverted ρV_p in Figure 9a; we do not expect a perfect match because Site 994 is ~ 1 km off line BT-1. Figure 10a shows the ρV_p inverted directly from the near-offset data set (Figure 2a) by the CSSI (acoustic inversion). Figure 10b shows the ρV_s inverted from EI and ρV_p (Figure 10a) using algorithm 3. The same constraints used in algorithm 2 are used in algorithm 3 in the inversion of ρV_s .

The ρV_p section estimated by algorithm 2 using EI (Figure 9a) is very similar to that estimated using the acoustic

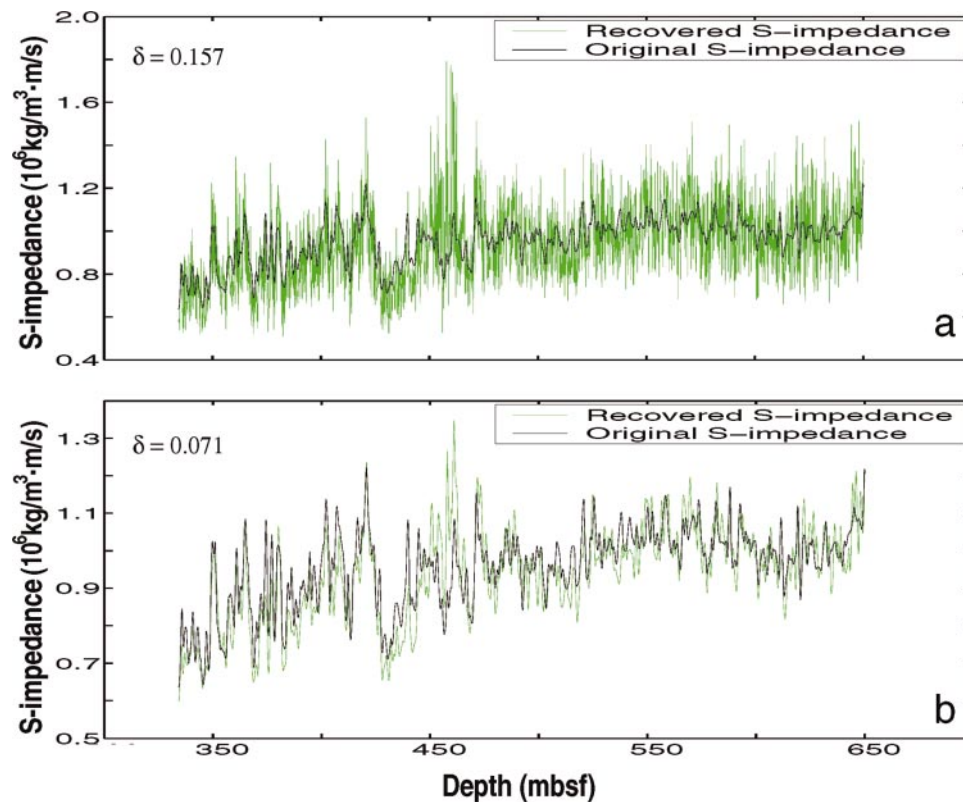


FIG. 6. Inverted ρV_s from EI with 7% random noise and noise-free ρV_p by using algorithm 3: (a) is the inverted ρV_s before smoothing, and (b) is after smoothing. Both the input EI and ρV_p were constructed from the well logs of Site 997. A 21-point triangular smoothing was used; δ is the standard deviation.

CSSI (Figure 10a). The two high-EI layers and the two low-EI layers observed in Figure 8 are related to two high- ρV_p layers and two low- ρV_p layers, respectively. The ρV_s from algorithm 2 (Figure 9b) is also similar to the ρV_s from algorithm 3 (Figure 10b). Algorithm 3 has only one unknown and is therefore more stable. From the previous tests with the well-log data, we see that the result from algorithm 3 is better. Thus, we use the ρV_s from algorithm 3 (Figure 10b) along with the ρV_p from the acoustic CSSI (Figure 10a) for further parameter estimation.

V_s/V_p and Poisson's ratio

From ρV_p and ρV_s , we can calculate the V_s/V_p ratio (Figure 11a),

$$\gamma = \frac{\rho V_s}{\rho V_p} = \frac{V_s}{V_p}, \quad (8)$$

and Poisson's ratio (Figure 11b),

$$\sigma = \frac{1 - 2\gamma^2}{2(1 - \gamma^2)}. \quad (9)$$

The two high ρV_p and ρV_s layers H1 and H2 show near background γ (slightly higher) and σ values (slightly lower); the σ values range from 0.41 to 0.43. These values indicate that the gas-hydrate concentration might be fairly low, and that the sediments are not cemented by gas hydrate (Katzman et al., 1994). The two low- ρV_p layers L1 and L2 show high γ and low σ ; the σ values range from 0.30 to 0.38, which is much higher than those (down to 0.1) for unconsolidated gas sand from labora-

tory measurements and theoretical analyses (Domenico, 1976; Gregory, 1976; Ostrander, 1984). These values, however, are similar to the result (0.3) obtained by Katzman et al. (1994) from AVO modeling and analysis of wide-angle ocean-bottom seismic data in this area, and are consistent with the results we calculated from the well logs at Sites 995B and 997. Two factors that may contribute to these high σ values are a relatively low V_s because of the very shallow depth (which is probably the main factor) and a relatively low free-gas concentration.

Lamé parameter terms

Goodway et al. (1997) showed that the Lamé parameter terms $\lambda\rho$, $\mu\rho$, and λ/μ calculated from ρV_p and ρV_s can be great pore fluid indicators. We show $\lambda\rho$ and λ/μ in Figure 12. The two inferred free-gas layers (L1 and L2) appear as low values in the $\lambda\rho$ section. The two gas-hydrate layers (H1 and H2) show relatively high $\lambda\rho$ values. The λ/μ section (Figure 12b) is somewhat similar to the σ section (Figure 11b); L1 and L2 have low λ/μ values, while H1 and H2 have λ/μ values slightly lower than the background values. Figure 12b shows values of λ/μ as high as 19, which is very high compared to those of Goodway et al. (1997) but are consistent with shallow unconsolidated sediments. These high λ/μ values correspond to low ρV_s layers (Figure 10b).

Estimation of gas-hydrate and free-gas concentration

To relate the inverted elastic properties to sediments containing gas hydrate or free gas, we also need to estimate the

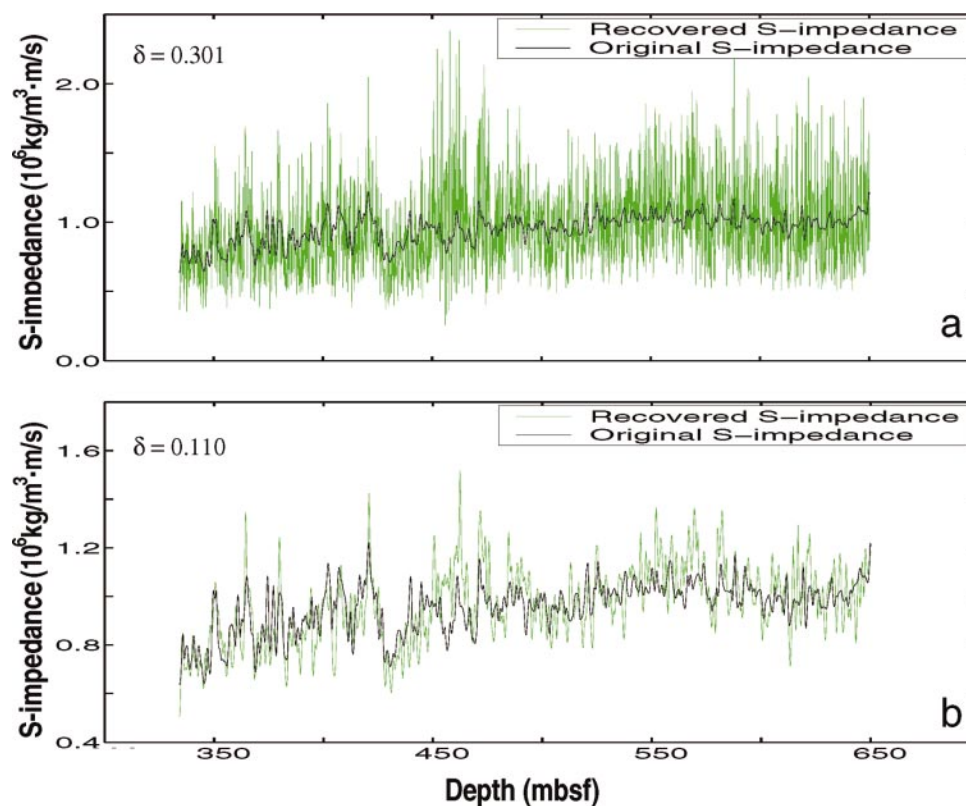


FIG. 7. Inverted ρV_s using algorithm 3 [equation (7)] after adding 7% random noise to both EI and ρV_p : (a) is the inverted ρV_s before smoothing, and (b) is after smoothing. Both the EI and ρV_p were constructed from the well logs of Site 997. A 21-point triangular smoothing was used; δ is the standard deviation.

distribution and concentration of gas hydrate and free gas, which we do here using the procedures in Lu and McMechan (2002). Empirical relations between acoustic impedance and water-filled porosity are developed by using well-log data from Hole 995B. The water-filled porosity (as inferred from the resistivity log) is calibrated to acoustic impedance twice: one calibration is applicable where free gas is present, and the other, where gas hydrate or water is present, so free-gas layers have to be identified before the calibrations are applied. To delineate the free-gas zones in the ρV_p section (Figure 10a), we first define the background trends of EI and σ by using well logs. Points that have values less than the trends of EI (Figure 8) by more than $0.80 \times 10^6 \text{ kg/m}^2/\text{s}$ and of σ (Figure 11b) by more than 0.06 are considered to be free-gas points. After the free-gas layers are identified, the water-filled porosity (Figure 13a) is estimated from the ρV_p (Figure 10a). The water-filled porosity decreases by compaction from $\sim 76\%$ near the sea floor to

$\sim 50\%$ at the bottom of the section, and has the lowest value of $\sim 45\%$ in layer H2; local reductions in water-filled porosity are consistent with gas hydrate or free gas in the pores (Lu and McMechan, 2002).

A combination of Archie equations is used to estimate gas-hydrate and free-gas saturation and concentration from the water-filled porosity (Lu and McMechan, 2002). The resulting combined estimate of the gas hydrate and free-gas concentrations is shown in Figure 13b. Figure 13c shows only the gas-hydrate concentration; Figure 13d shows only the free-gas concentration.

INTERPRETATION AND DISCUSSION

After obtaining the elastic properties and the gas-hydrate and free-gas concentrations, we can now interpret the results. For clarity of the explanations, we expand a window (Figure 14) near the center of some of the previously shown sections.

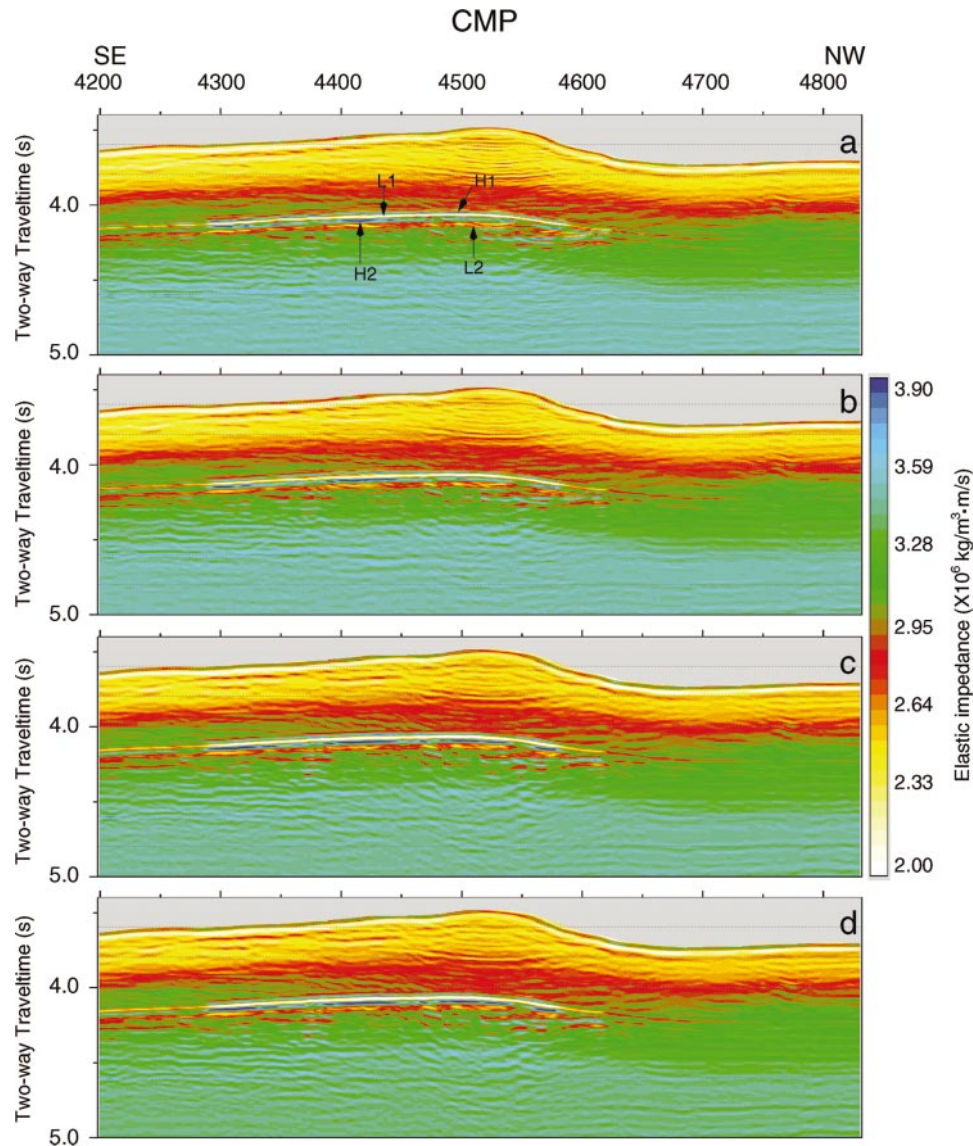


FIG. 8. Inverted EI obtained from the EI inversion of the CAA data sets shown in Figure 2: (a) 0° – 8° , (b) 8° – 16° , (c) 16° – 24° , and (d) 24° – 32° . “L1” and “L2” are two low-EI layers; “H1” and “H2” are two high-EI layers.

The concentration and distribution of gas hydrate and free gas

Three gas hydrate layers (H0, H1, and H2) are interpreted (Figures 13c and 14a). Layer H0 has an estimated average concentration of 3–5.5% by volume. Between layers H0 and H1, there is a gap with no (or very low) gas-hydrate concentration. This gap becomes thicker and penetrates layer H0 toward the local topographic high in the sea floor. Layer H1 has gas-hydrate concentration ranging between 3% and 8% by volume. The gas hydrate in layer H2 is less continuous than that of layer H1, has a concentration less than 1% at some places, and attains the highest values of 9% at others. All these gas-hydrate concentrations correspond to less than 20% of the estimated

porosities. Thus, the hydrate does not saturate the pores, and so produces locally reduced permeability, but not a flow barrier.

Free gas (Figures 13d and 14b) in layers L1 and L2 has an estimated average concentration of 3–8% by volume, and has the highest values near the local topographic high in the sea floor. The free-gas concentration in layer L1 decreases away from the topographic high to near zero toward right end of the section, although gas hydrates are still well developed there. Comparing this free-gas distribution to the behavior of the seismic BSR (Figure 2), explains the BSRs as being caused by the presence of free gas in this area. Free gas in layers L1 and L2 is concentrated by the overlying reduced permeability hydrate layers (H1 and H2, respectively). The upward curvature

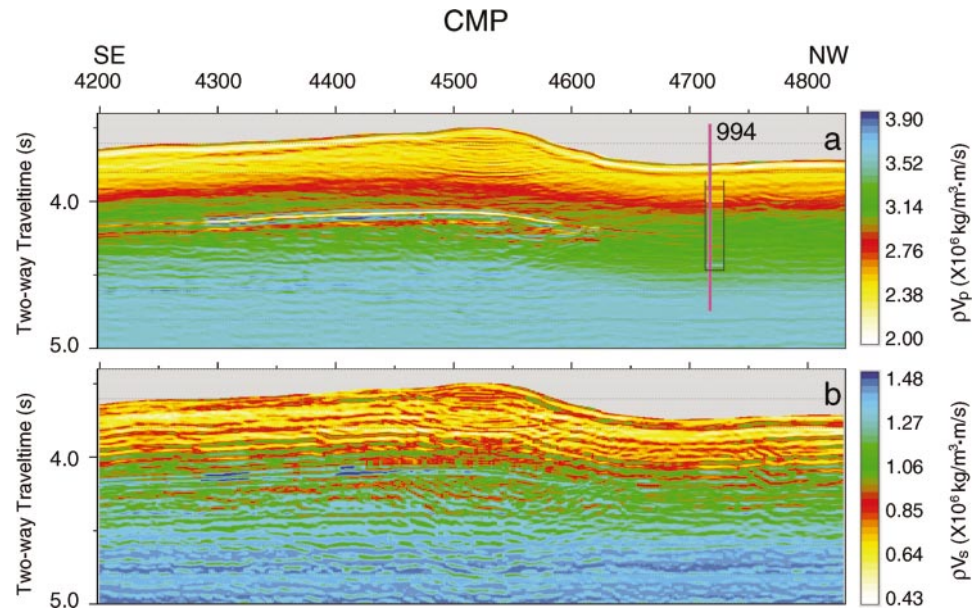


FIG. 9. Inverted (a) ρV_p section overlain with the ρV_p projected from Site 994 and (b) ρV_s sections. (a) and (b) are obtained from the EI sections shown in Figure 8 using algorithm 2.

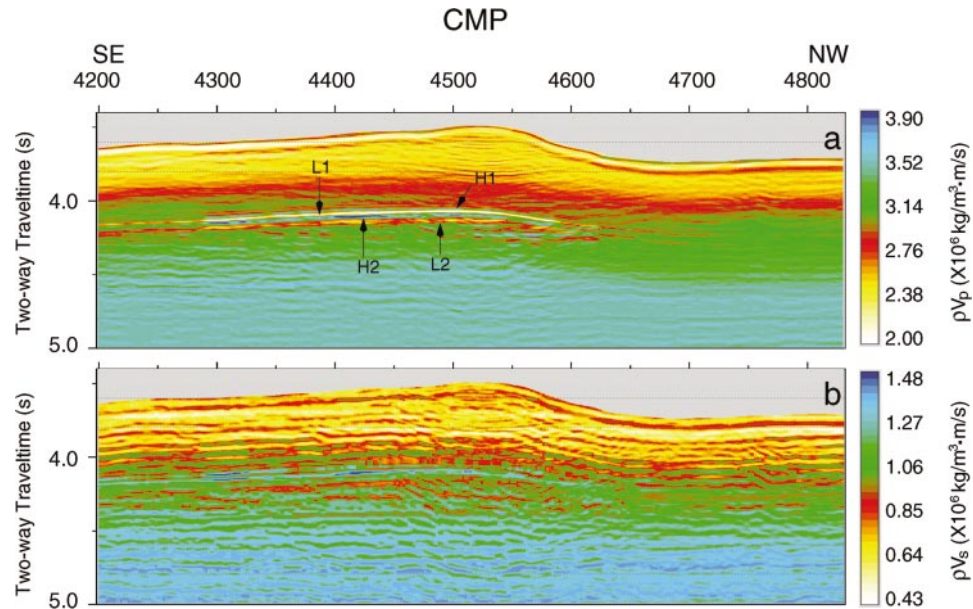


FIG. 10. (a) The inverted ρV_p from the near offset angle data set (Figure 2a) by acoustic CSSI. (b) The ρV_s inverted from the EI sections (Figure 8) and the ρV_p section (a) using algorithm 3.

of H1 and H2 (following the sea floor) provides the closure that concentrates the gas. The lack of continuity of H0 at its shallowest depth provides an escape conduit that explains the lack of free gas inside the gap between layers H0 and H1. As with the gas hydrate, the gas concentration is insufficient to completely saturate the pores.

Discontinuous free gas is distributed beneath layer L2 near the center of the section and has an average free-gas concentration of only 1–3% by volume. In some places, free-gas layers are not present immediately below the gas-hydrate layers (Figure 13b). These vertical gaps are very small compared to those mentioned by Xu and Ruppel (1999) and by Kastner (2001), which can be as large as tens of meters, and may be explained by the methane flux rate or the supply of methane. The

deeper free-gas areas appear to conform to the stratigraphic geometry rather than the gas hydrate geometry, which is expected when hydrate is not present. Our estimates of gas-hydrate and free-gas concentrations are consistent with those from the well logs of ODP Leg 164 (Paull and Matsumoto, 2000), which show that gas hydrates occupy ~1–10% of the sediment volume in a zone that is at least 250-m thick, and that the free gas has a concentration ranging between 1 and 12% below the BSR (Dickens et al., 1997).

The effects of free gas and gas hydrate on elastic properties

When sediments contain even small quantities of free gas, V_p drops dramatically, while V_s changes little (Domenico, 1976).

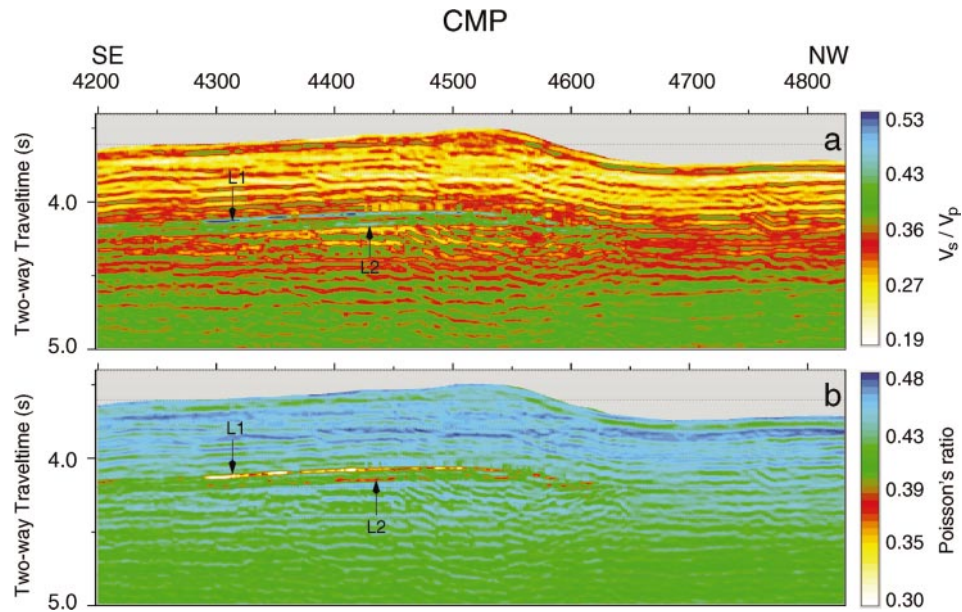


FIG. 11. (a) The V_s/V_p section and (b) The σ section estimated from the ρV_p and ρV_s sections in Figure 10.

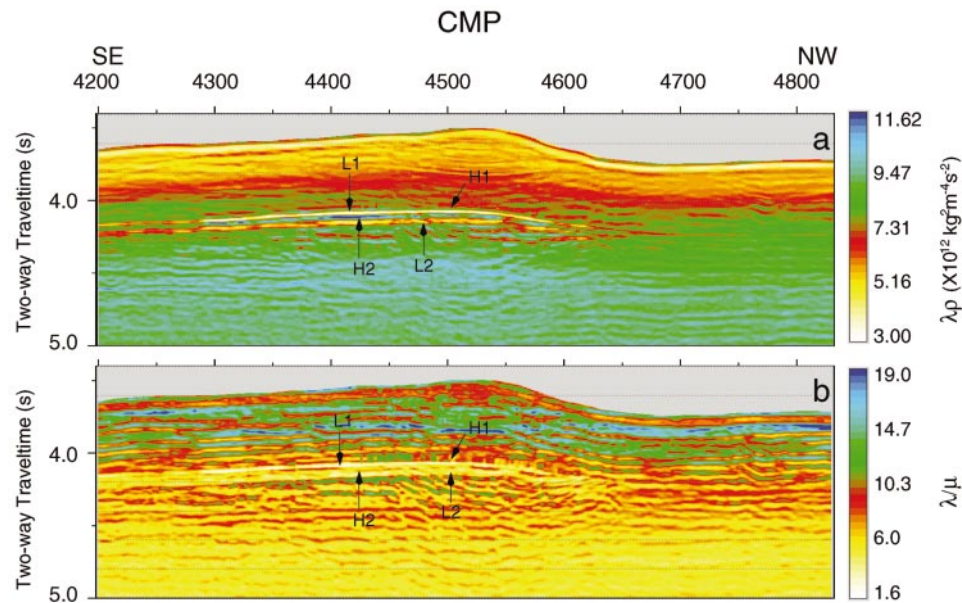


FIG. 12. (a) The $\lambda\rho$ section and (b) The λ/μ section estimated from the ρV_p and ρV_s sections in Figure 10.

Thus, free-gas layers L1 and L2 have high γ (Figure 11a) and low σ (Figures 11b and 14e) values; γ and σ have been widely used to identify gas layers. When the gas-hydrate concentration is low (which is the case here), the sediments are not cemented, and both V_p and V_s will increase, which results in a nonanomalous or slightly lower σ value compared to unhydrated sediments (Tinivella and Accaino, 2000). So σ , along with γ and $\mu\rho$, cannot be used alone to distinguish the hydrated sediments from the unhydrated sediments. On the other hand, when gas-hydrate concentration is fairly high, the hydrated sediments will be cemented by gas hydrate, and so are expected to resist shear traction better. Therefore, V_s will increase faster than V_p (Katzman et al., 1994; Kunerth et al., 2001), and σ will decrease.

When gas-hydrate concentration is sufficiently high, the hydrated sediments may have lower σ than the free-gas charged sediments [See Figure 10 of Tinivella and Accaino

(2000)]. Thus, σ can not be used to differentiate between hydrated sediments and free-gas charged sediments when gas hydrate concentration is very high and when free-gas concentration is very low, although it helps identify gas-hydrate and free-gas zones.

Faulting and fluid flow

The gas-hydrate/free-gas system as a whole is a dynamic system (Holbrook, 2001) in which fluid flow plays an important role. Fluid migration is more active in complex structural zones (Hovland et al., 1997; Cunningham and Lindholm, 2000) where faults and dipping stratigraphy may facilitate water and gas migration.

The right end of the section (Figure 2) is close to the ridge-collapse structure, inside of which normal faults are common

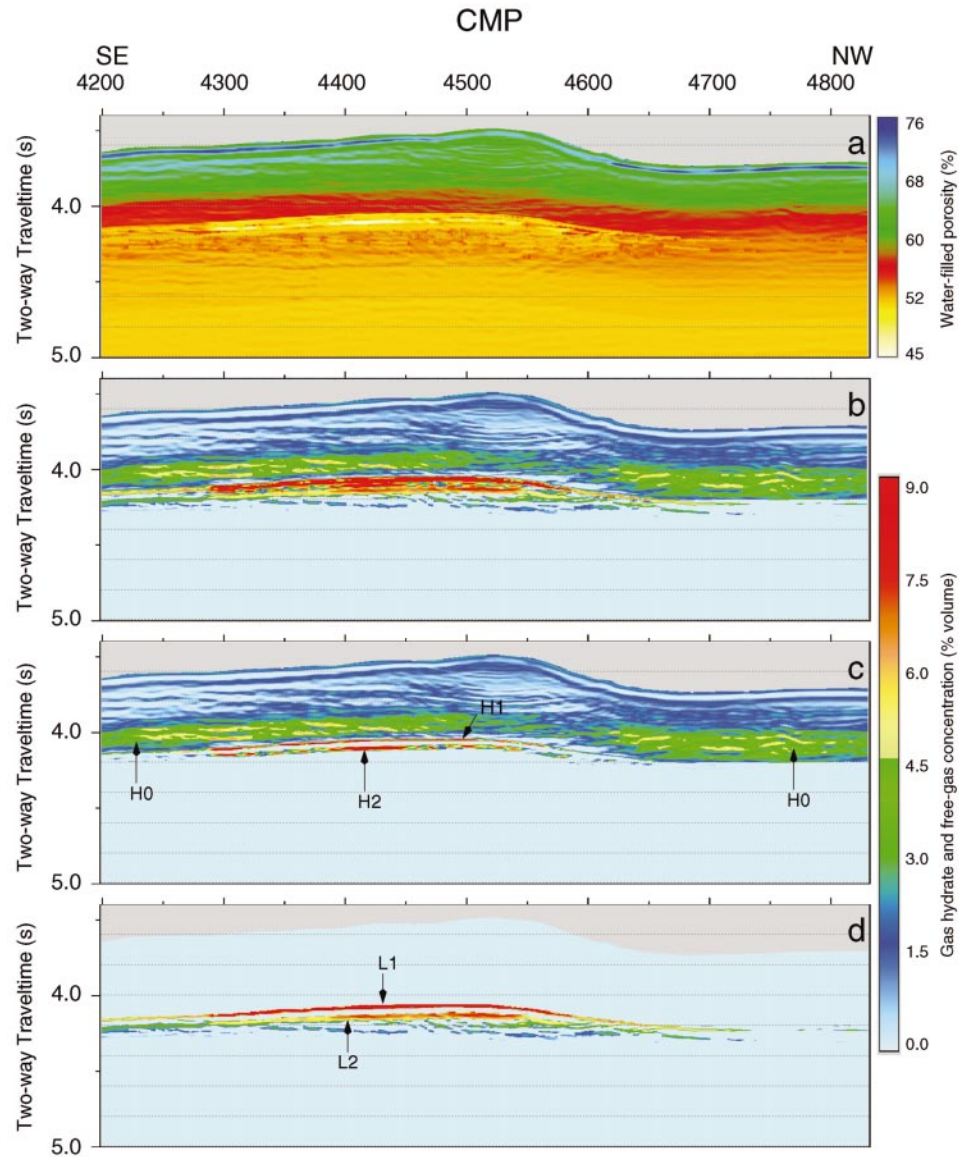


FIG. 13. (a) Water-filled porosity, (b) gas-hydrate and free-gas concentration, (c) gas-hydrate concentration, and (d) free-gas concentration.

and provide pathways for the escape of free gas and for fluid transport (Dillon et al., 2001; Holbrook, 2001). This may explain the lack of free gas below the gas-hydrate layer H0 at the right end of the section (Figure 13d).

Near the local sea-floor topographic high, the ρV_s (Figures 10a and 14d), γ (Figure 11a), σ (Figures 11b and 14e), $\lambda\rho$ (Figures 12a and 14f), and $\mu\rho$ (Figure 12b) sections show that the layers are somewhat laterally discontinuous, suggesting the presence of high-angle faults. These faults may act as conduits for fluid flow. At the local topographic high, the fluid flow is expected to be the most active, and may be the cause of the gap in H0 which, in turn, provides a path of escape for any free gas that may have been present between H0 and H1 (as there is apparently no gas there now).

GHSZs and BSRs

Since the sediments have a fairly homogeneous lithology composed of calcareous nannofossil-rich clay and claystones (Paull et al., 1996; Paull and Matsumoto, 2000), the separation of gas-hydrate layers H0, H1, and H2 suggests that each layer corresponds to a different stability condition. The presence of 3% ethane and 1% propane in gas hydrates can result in a shift of the base of the GHSZ to ~ 50 m deeper compared to gas hydrate of 100% methane [see Figure 7 of Andreassen et al. (2000)]. Thus, different GHSZs are expected to be present for gas-hydrates with different hydrocarbon molecules. As a consequence, we speculate that there may be gas hydrates of three different compositions present. The triple gas-hydrate

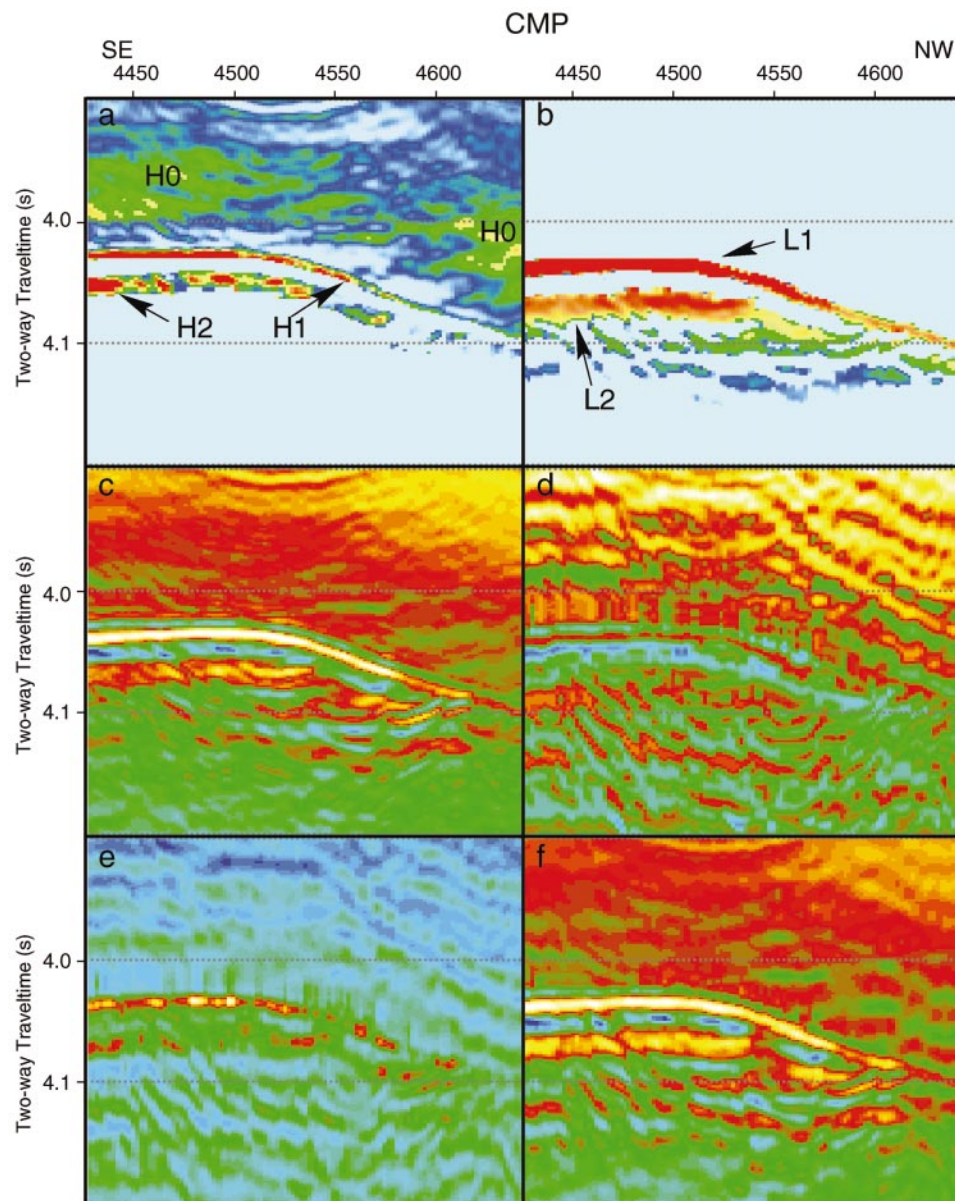


FIG. 14. Expanded views of sections (a) gas-hydrate concentration, (b) free-gas concentration, (c) ρV_p , (d) ρV_s , (e) σ , and (f) $\lambda\rho$.

layers are explained if H0 contains gas hydrates of the lightest hydrocarbon molecules (mainly methane), H1 and L1 contain hydrocarbon of heavier molecules than in layer H0 (but lighter than that of layer H2), and H2, L2, and the layers below L2 have the heaviest hydrocarbon molecules. This seismic interpretation is consistent with the geochemical analysis of data from Sites 994, 995, and 997 (Wehner et al., 2000), which found that gases from these sites are a mixture of methane (inferred to have a predominantly microbial origin) and ethane and propane (inferred to have a predominantly thermal origin). There may also be some physical separation involved, with the lighter (physically smaller and more mobile) molecules that are dissolved in the water percolating more easily through the low-permeability section to the shallower depths than the larger, heavier molecules. Gas concentration in excess of the solubility in water leads to the formation of bubbles, whose transport by water flow is retarded when the size of the bubbles exceeds the size of the pore throats in the sediments. Thus even a slightly reduced permeability associated with gas hydrate facilitates the concentration of free-gas beneath it (Andreassen et al., 1997).

The free-gas in layer L1 corresponds to the conventional definition of the BSR. This BSR marks the boundary between H1 and L1, and, therefore, the base of the second GHSZ. Free-gas trapped in layer L2 produces a second BSR, which marks the boundary between H2 and L2 and, therefore, the base of the third GHSZ. The vertical distance between the conventional BSR and this second BSR is much shorter than that of observed by Tréhu et al. (1999) and Andreassen et al. (2000), and is difficult to discern from the seismic section (Figure 2) before inversion.

The presence of gas hydrate below the BSR

Our multiple hydrate-layer interpretation based on gas composition is consistent with a model that includes gas hydrate beneath the conventional BSR in this area. Based on the lack of chloride anomalies below the BSR, Paull et al. (1996) and Egeberg and Dickens (1999) concluded that gas hydrates are present only above the BSR in the Blake Ridge. It is also true that no high P-wave velocity layer beneath the BSR was observed in waveform inversion in the Blake Ridge (Korenaga et al., 1997; Holbrook, 2001), but this technique might not have enough resolution to identify this gas-hydrate layer. On the other hand, Guérin et al. (1999) concluded from observation of a high-compressibility formation beneath the BSR and attenuation of the monopole sonic waveform in well-logs from Site 995 that hydrates and free gas coexist in this formation. They explained the coexistence of gas hydrates and free gas by capillary effects in the small pores or by remaining crystalline structures after partial hydrate dissociation.

The drilling results of ODP Leg 164 (Paull et al., 1996) show that there is a discrepancy between the observed seismic depth of the BSR and the thermodynamically predicted base of the GHSZ at Sites 995 and 997. Paull et al. (1996) suggested three possible explanations for the depth discrepancy, all of which are at least in part compatible with the interpretation of multiple GHSZs. The first proposed explanation was that the present BSR perhaps is not in equilibrium because of changing water depth or temperature. There is no seismic evidence for changing water depth, but the simultaneous presence of different GHSZs for different gas compositions certainly could mimic a

change of thermodynamic conditions with time. The second proposed explanation was that the conditions of formation of hydrate in fine-grained sediments are not sufficiently well understood to make quantitative predictions; Kraemer et al. (2000) and Ruppel (1997) suggest that capillary action inhibits the formation of gas hydrate in small pore spaces. This is consistent with Paull et al.'s (1996) uncertainty in what controls the BSR locations in fine-grained sediments, and with the idea that the lighter gas molecules can move more easily than the heavier molecules through small pore spaces to the shallower depths. The third proposed explanation was that gas hydrate may be present below the BSR but was not detected. This is supported by gas-hydrate occurrence (documented in the core photos) below the BSR, subsequently reported by Lorenson and Collett (2000) and by Lorenson and the Leg 164 Shipboard Scientific Party (2000). With the interpretation of multiple GHSZs and low gas-hydrate concentration, it is easy to understand the apparent depth discrepancy. Thus, the conventional BSR marks the top of free gas occurrence (Guérin et al., 1999) and the base of one of the series of GHSZs. This model can be checked by detailed geochemical analysis of the composition of the free gas and gas hydrate as a function of depth, but a definitive conclusion is not yet possible at this time.

CONCLUSIONS

We have inverted time-migrated CAA data sets to give EI data sets. The hydrated sediments show relatively high EI values, while the free-gas charged layers show relatively low EI values. The magnitude of the EI of hydrated sediments and free-gas charged layers changes with incident angle.

We have developed and evaluated methods to estimate ρV_p and ρV_s from EI. Our new methods provide good estimation of ρV_p and ρV_s from EI for any reasonable $K (= V_s^2/V_p^2)$. Smoothing improves the estimation of ρV_p and ρV_s when noise is present. Hydrated sediments have relatively high ρV_p and ρV_s , whereas the free-gas charged layers have low ρV_p and nonanomalous background ρV_s .

The σ estimated from the ρV_p and ρV_s shows low values in free-gas charged layers and near-background values in hydrated sediments, suggesting that the gas-hydrate concentration is fairly low. The σ alone can not differentiate between hydrated sediments and free-gas charged layers when gas hydrate concentration is high, and can not differentiate between hydrated sediments and nonhydrated sediments when gas hydrate concentration is low. The σ in the free-gas charged layers has relatively high values compared to laboratory measurements and theoretical analyses. Two factors contribute to this: one is the relatively low V_s or ρV_s , and the other is the relatively low free-gas concentration.

The Lamé parameter term $\lambda\rho$ shows relatively high values in hydrated sediments, but relatively low values in free-gas charged layers; λ/μ shows behavior similar to that of σ in that it has low values in the free-gas charged sediments and near-background values in the hydrated sediments. The relatively low ρV_s leads to the relatively high λ/μ .

In our study area, gas hydrates and free gas are both estimated to have concentrations of 1–8% by volume. Free gas is well developed in layers L1 and L2 beneath the topographic high of the sea floor. Gas hydrate is interpreted to be present in three layers (H0, H1, and H2), suggesting three chemically

distinct gas components and the corresponding presence of three GHSZs. Each gas hydrate layer is interpreted to contain gas of progressively increasing molecular weight with increasing depth. The conventional BSR marks only the top of free-gas and the base of one of the series of GHSZs.

ACKNOWLEDGMENTS

The research leading to this paper was funded by the sponsors of the UT-Dallas Geophysical Consortium, by the Petroleum Research Fund of the American Chemical Society through grant 36706-AC, and by the Texas Advanced Research Program through grant 9741-0038-2001. We thank Myung W. Lee of the U.S. Geological Survey for providing the seismic data, and David Goldberg of Lamont-Doherty Earth Observatory of Columbia University for his V_s log. We also gratefully acknowledge Geocenter for the SeisUP seismic processing software, and Jason Geosystems for the inversion software. This paper is contribution No. 1002 from the Department of Geosciences at the University of Texas at Dallas.

REFERENCES

- Andreassen, K., Hart, P. E., and MacKay, M., 1997, Amplitude versus offset modeling of the bottom simulating reflection associated with submarine gas hydrates: *Marine Geology*, **137**, 25–40.
- Andreassen, K., Mienert, J., Bryn, P., and Singh, S. C., 2000, A double gas-hydrate related bottom simulating reflectors at the Norwegian continental margin, in Holder, G.D., and Bishnoi, P.R., Eds., *Gas hydrates challenges for the future: Annals of the New York Academy of Sciences*, **912**, 126–135.
- Cambois, G., 2000, AVO inversion and elastic impedance: 70th Annual International Meeting, Society of Exploration Geophysicists, Expanded Abstracts, 142–145.
- Claerbout, J. F., and Muir, F., 1973, Robust modeling with erratic data: *Geophysics*, **38**, 826–844.
- Collett, T. S., and Ladd, J., 2000, Detection of gas hydrate with downhole logs and assessment of gas hydrate concentrations (saturations) and gas volumes on the Blake Ridge with electrical resistivity log data: *Proceedings of the Ocean Drilling Program, Scientific Results*, **164**, 179–191.
- Connolly, P., 1999, Elastic impedance: *The Leading Edge*, **18**, 438–452.
- Cunningham, R., and Lindholm, R. M., 2000, Seismic evidence for widespread gas hydrate formation, offshore west Africa, in Mello, M.R., and Katz, B.J., Eds., *Petroleum system of South Atlantic margins: American Association of Petroleum Geologists Memoir* **73**, 93–105.
- Dickens, G. R., Paull, C., Wallace, P., and the ODP Leg 164 Scientific Party, 1997, Direct measurements of in situ methane quantities in a large gas-hydrate reservoir: *Nature*, **385**, 427–429.
- Dillon, W. P., Nealon, J. W., Taylor, M. H., Lee, M. W., Drury, R. M., and Anton, C. H., 2001, Seafloor collapse and methane venting associated with gas hydrate on the Blake Ridge—Causes and implications to seafloor stability and methane release, in Paull, C.K., and Dillon, W.P., Eds., *Natural gas hydrates: occurrence, distribution, and detection: American Geophysical Union Geophysical Monograph* **124**, 211–233.
- Domenico, S. N., 1976, Effect of brine-gas mixture on velocity in an unconsolidated sand reservoir: *Geophysics*, **41**, 882–894.
- Egeberg, P. K., and Dickens, G. R., 1999, Thermodynamic and pore water halogen constraints on gas hydrate distribution at ODP Site 997 (Blake Ridge): *Chemical Geology*, **153**, 53–79.
- Goodway, W., Chen, T., and Downton, J., 1997, Improved AVO fluid detection and lithology discrimination using Lamé petrophysical parameters; “ $\lambda\rho$,” “ $\mu\rho$,” “ λ/μ fluid stack,” from P and S inversions: 67th Annual International Meeting, Society of Exploration Geophysicists, Expanded Abstracts, 183–186.
- Grauls, D., 2001, Gas hydrates: Importance and applications in petroleum exploration: *Marine Petroleum Geology*, **18**, 519–523.
- Gregory, A. R., 1976, Fluid saturation effects on dynamic elastic properties of sedimentary rocks: *Geophysics*, **41**, 895–921.
- Guérin, G., Goldberg, D., and Meltser, A., 1999, Characterization of in situ elastic properties of gas hydrate-bearing sediments on the Blake Ridge: *Journal of Geophysical Research*, **104**, 17,781–17,795.
- Helgesen, J., Magnus, I., Prosser, S., Saigal, G., Aamodt, G., Dolberg, D., and Busman, S., 2000, Comparison of constrained sparse spike and stochastic inversion for porosity prediction at Kristin field: *The Leading Edge*, **19**, 400–407.
- Holbrook, W. S., 2001, Seismic studies of the Blake Ridge: Implications for hydrate distribution, methane expulsion, and free gas dynamics, in Paull, C.K., Dillon, W.P., Eds., *Natural gas hydrates: occurrence, distribution, and detection: American Geophysical Union Geophysical Monograph* **124**, 235–256.
- Hovland, M. J., Gallagher, J. W., Clenell, M. B., and Lekvan, K., 1997, Gas hydrate and free gas volumes in marine sediments: Example from the Niger Delta front: *Marine Petroleum Geology*, **14**, 245–255.
- Jason Geosystems, 1999, Trace-based inversion and modeling training manual: Jason Geosystems.
- Kastner M., 2001, Gas hydrates in convergent margins: Formation, occurrence, geochemistry, and global significance, in Paull, C.K., Dillon, W.P., Eds., *Natural gas hydrates: occurrence, distribution, and detection: American Geophysical Union Geophysical Monograph* **124**, 67–86.
- Katzman, R., Holbrook, W. S., and Paull, C. K., 1994, Combined vertical-incidence and wide-angle seismic study of a gas hydrate zone, Blake Ridge: *Journal of Geophysical Research*, **99**, 17,975–17,995.
- Korenga, J., Holbrook, W. S., Singh, S. G., and Minshull, T. A., 1997, Natural gas hydrates on the southeast U.S. margins: Constraints from full wave form and travel time observations of wide-angle seismic data: *Journal of Geophysical Research*, **102**, 15 345–15 365.
- Kraemer, L. M., Owen, R. M., and Dickens, G. R., 2000, Lithology of the upper gas hydrate zone, Blake Outer Ridge: A link between diatoms, porosity, and gas hydrate: *Proceedings of the Ocean Drilling Program, Scientific Results*, **164**, 229–236.
- Kunert, D. C., Weinberg, D. M., Rector, J. W., Scott, C. L., and Johnson, J.T., 2001, Acoustic laboratory measurements during the formation of a THF-hydrate in unconsolidated porous media: *Journal of Seismic Exploration*, **9**, 337–354.
- Kvenvolden, K. A., 1998, A primer on the geological occurrence of gas hydrate, in Henriot, J.-P., and Mienert, J., Eds., *Gas Hydrates—Relevance to world margin stability and climatic change: Geological Society of London Special Publication* **137**, 9–30.
- Laherrère, J. H., 2000, Oceanic hydrates: more questions than answers: *Energy Exploration and Exploitation*, **18**, 349–383.
- Lee, M. W., Hutchinson, D. R., Agena, W. F., Dillon, W. P., Miller, J. J., and Swift, A. B., 1994, Seismic character of gas hydrates on the southeastern U.S. continental margin: *Marine Geophysical Research*, **16**, 163–184.
- Lee, M. W., Hutchinson, D. R., Dillon, W. P., Miller, J. J., Agena, W. F., and Swift, A. B., 1993, Method of estimating the amount of in-situ gas hydrates in deep marine sediments: *Marine Petroleum Geology*, **10**, 493–506.
- Lorenson, T. D., and Collett, T. S., 2000, Gas content and composition of gas hydrate from sediments of the Southeastern North American continental margin: *Proceedings of the Ocean Drilling Program, Scientific Results*, **164**, 37–46.
- Lorenson, T. D., and the Leg 164 Shipboard Scientific Party, 2000, Graphic summary of gas hydrate occurrence by proxy measurements across the Blake Ridge, Sites 994, 995 and 997: *Proceeding of the Ocean Drilling Program, Scientific Results*, **164**, 247–248.
- Lu, S., and McMechan, G. A., 2002, Estimation of gas hydrate and free gas saturation, concentration, and distribution from seismic data: *Geophysics*, **67**, 582–593.
- Mallick, S., 2001, AVO and elastic impedance: *The Leading Edge*, **20**, 1094–1104.
- Mallick, S., Huang, X., Lauve, J., and Ahmad, R., 2000, Hybrid seismic inversion: A reconnaissance tool for deepwater exploration: *The Leading Edge*, **19**, 1230–1251.
- Matsumoto, R., 2000, Methane hydrate estimates from the chloride and oxygen isotopic anomalies, in Holder, G.D., and Bishnoi, P.R., Eds., *Gas hydrates challenges for the future: Annals of the New York Academy of Sciences* **912**, 39–50.
- Menke, W., 1984, Geophysical data analysis: Discrete inverse theory: Academic Press.
- Ostrander, W. J., 1984, Plane-wave reflection coefficients for gas sands at non-normal angles of incidence: *Geophysics*, **49**, 1637–1648.
- Paull, C. K., and Matsumoto, R., 2000, Leg 164 overview: *Proceedings of the Ocean Drilling Program, Scientific Results*, **164**, 3–10.
- Paull, C. K., Matsumoto, R., Wallace P. J., and the Leg 164 Scientific Party, 1996, *Proceedings of the Ocean Drilling Program, Initial Reports*, **164**, 1–318.
- Ruppel, C., 1997, Anomalously cold temperatures observed at the base of the gas hydrate stability zone on the U.S. Atlantic passive margin: *Geology*, **25**, 669–702.
- Savic, M., Verwest, B., Masters, R., Sena, A., and Gingrich, D., 2000, Elastic impedance inversion in practice: 70th Annual International Meeting, Society of Exploration Geophysicists, Expanded Abstracts, 689–692.

- Sloan, E. D., 1998a, Clathrate hydrate of natural gas, 2nd ed.: Marcel Dekker.
- 1998b, Physical/chemical properties of gas hydrates and application to world margin stability and climatic change, in Henriet, J.-P., and Mienert, J., Eds., Gas hydrates—Relevance to world margin stability and climatic change: Geological Society of London Special Publication, **137**, 31–50.
- Tinivella, U., and Accaino, F., 2000, Compressional velocity structure and Poisson's ratio in marine sediments with gas hydrate and free gas by inversion of reflected and refracted seismic data (South Shetland Islands, Antarctica): Marine Geology, **164**, 13–27.
- Tinivella, U., and Lodolo, E., 2000, The Blake Ridge bottom-simulating reflector transect: Tomographic velocity field and theoretical model to estimate methane hydrate quantities: Proceedings of the Ocean Drilling Program, Scientific Results, **164**, 273–281.
- Tréhu, A. M., Torres, M. E., Moore, G., Suess, E., and Bohrmann, G., 1999, Temporal and spatial evolution of a gas hydrate-bearing accretionary ridge on the Oregon continental margin: Geology, **27**, 939–942.
- Wehner, H., Faber, E., and Hufnagel, H., 2000, Characterization of low and high molecular-weight hydrocarbons in sediments from the Blake Ridge, sites 994, 995 and 997: Proceedings of the Ocean Drilling Program, Scientific Results, **164**, 47–58.
- Whitcombe, D.N., 2002, Elastic impedance normalization: Geophysics, **67**, 60–62.
- Xu, W., and Ruppel, C., 1999, Predicting the occurrence, distribution, and evolution of methane gas hydrate in porous marine sediments: Journal of Geophysical Research, **104**, 5081–5095.

APPENDIX A

ALGORITHM 2: ESTIMATION OF ρV_p AND ρV_s FROM EI

In equation (4), if we make a first-order approximation by using the small-angle approximation $\tan^2\theta \approx \sin^2\theta$, we have

$$\ln(EI) \approx (1 + \sin^2\theta) \ln(V_p) - 8K \sin^2\theta \ln(V_s) + (1 - 4K \sin^2\theta) \ln(\rho). \quad (\text{A-1})$$

Our testing with well-log data shows that this approximation has little affect on the estimation of ρV_p , but makes the estimation of ρV_s very unstable [when we solve for V_s in equation (A-1), the coefficient of V_s is close to zero when the incidence angle is small]. Even with no noise in the input EI, the inverted ρV_s can become unrealistically large for small incident angles. So a further constraint has to be included.

Cambois (2000) and Mallick (2001) assumed a background V_p/V_s ratio of 2 (i.e. $K = 0.25$). Then, equation (A-1) becomes

$$\ln(EI) \approx \ln(\rho V_p) + [\ln(\rho V_p) - 2 \ln(\rho V_s)] \sin^2\theta. \quad (\text{A-2})$$

Mallick (2001) showed that equation (A-2) gives results similar to those obtained from his hybrid inversion. However, the as-

sumption of $K = 0.25$ is not valid for our data. We have $K \approx 0.10$ because of the relatively low V_s . Equation (A-2) leads to a large difference between the inverted and the original ρV_s and so fails the requirement of being able to provide reasonable estimates when the correct solution is known. The empirical approximation

$$4K \sin^2\theta \ln(\rho) \approx \sin^2\theta \ln(\rho) - 6K(0.25 - K) \left(\frac{1}{aK} - \frac{K}{b} \right) \sin^2\theta \quad (\text{A-3})$$

is used to reduce the difference. Then, we get equation (6) using equations (A-1) and (A-3). For K less than 0.25, $a = 8.0$ and $b = 0.5$; for K larger than 0.25, $a = 3.0$ and $b = 3.0$. Equation (A-3) gives a reasonable approximation for any reasonable K value (0.0–0.8). Equation (6) is identical to equation (A-2) only when $K = 0.25$, but it provides a better estimation of ρV_s than equation (A-2) for any other K value (0.0–0.8).